Computer Methods in Biomechanics and Biomedical Engineering: Imaging & Visualization

ISSN: (Print) (Online) Journal homepage: www.tandfonline.com/journals/tciv20

Quantifying and Visualizing Uncertainty for Source Localisation in Electrocardiographic Imaging

Dennis K. Njeru, Tushar M. Athawale, Jessie J. France & Chris R. Johnson

To cite this article: Dennis K. Njeru, Tushar M. Athawale, Jessie J. France & Chris R. Johnson (2023) Quantifying and Visualizing Uncertainty for Source Localisation in Electrocardiographic Imaging, Computer Methods in Biomechanics and Biomedical Engineering: Imaging & Visualization, 11:3, 812-822, DOI: 10.1080/21681163.2022.2113824

To link to this article: https://doi.org/10.1080/21681163.2022.2113824

Published online: 12 Sep 2022.

COMPUTER METHODS IN BIOMECHANICS AND BIOMEDICAL ENGINEERING: IMAGING & VISUALIZATION
2023, VOL. 11, NO. 3, 812–822
https://doi.org/10.1080/21681163.2022.2113824

Taylor & Francis
Taylor & Francis Group

Quantifying and Visualizing Uncertainty for Source Localisation in Electrocardiographic Imaging

Dennis K. Njeru[a], Tushar M. Athawale[b], Jessie J. France[a] and Chris R. Johnson[a]

[a]Scientific Computing and Imaging (SCI) Institute, University of Utah, Salt Lake City, UT, USA; [b]Oak Ridge National Laboratory, Oak Ridge, TN, USA

ABSTRACT

Electrocardiographic imaging (ECGI) presents a clinical opportunity to noninvasively understand the sources of arrhythmias for individual patients. To help increase the effectiveness of ECGI, we provide new ways to visualise associated measurement and modelling errors. In this paper, we study source localisation uncertainty in two steps: First, we perform Monte Carlo simulations of a simple inverse ECGI source localisation model with error sampling to understand the variations in ECGI solutions. Second, we present multiple visualisation techniques, including confidence maps, level-sets, and topology-based visualisations, to better understand uncertainty in source localization. Our approach offers a new way to study uncertainty in the ECGI pipeline.

ARTICLE HISTORY
Received 3 June 2021
Accepted 12 August 2022

KEYWORDS
Electrocardiographic imaging (ECGI); uncertainty visualisation; Monte Carlo simulation

1. Introduction

To rapidly diagnose heart disease, clinicians rely on the electrocardiogram (ECG), which records voltages on the torso surface. The voltages vary in response to changes in the heart's electrical activity. Although the ECG quickly provides clinicians with information on abnormal rhythms or *arrhythmias*, it cannot reveal localised high-resolution spatial information about the heart's electrical impulses.[1]

For example, in arrhythmias involving added abnormal beats, such as premature ventricular contraction (PVC), a region of cardiac tissue initiates pathological heartbeats, thereby increasing a patient's risk of sudden death (Messineo 1989). The lack of high-resolution spatial information from the ECG in locating this region is problematic, because one method of therapy involves a clinician locating and destroying the region through an invasive interventional procedure called catheter ablation. A catheter ablation procedure may last several hours with a frequently high rate of recurrence of the arrhythmia (O'Donnell et al. 2003; Arya et al. 2010).

Electrocardiographic imaging (ECGI) is one promising technique for increasing the speed and accuracy of ablation therapy. ECGI combines a patient's computed tomography (CT) and magnetic resonance imaging (MRI) images along with the ECG to create a functional imaging modality (Johnson 1997; Ghosh et al. 2008b; MacLeod et al. 2009; van der Graaf et al. 2014). Challenges in ECGI may be categorised as technical (e.g. regularisation, filtering techniques, and postprocessing methods), pathological (i.e. ability to extract features applicable to a specific pathology or arrhythmia), and clinical (i.e. benefits with respect to daily clinical practice) (Cluitmans et al. 2018). Our work addresses both the technical and clinical aspects of ECGI, with particular emphasis placed on using visualisation techniques to better understand ECGI simulation uncertainty and aid in clinical decision-making.

Whereas the ECG may be thought of as a forward problem that relates the heart's electrical activity to the recorded torso surface voltages, potential-based ECGI is the corresponding inverse problem that relates ECG measurements to heart surface voltages (Johnson 1997; Wang et al. 2011a; Rudy 2013). The mapping between the heart surface voltages and torso surface voltages may be written mathematically as

$$A\mathbf{h} + \mathbf{e} = \mathbf{y}, \tag{1}$$

where A is a transfer matrix relating the heart surface voltages $\mathbf{h}$ to the torso surface ECG recordings $\mathbf{y}$. The noise term $\mathbf{e}$ is modelled as a Gaussian distributed random variable to characterise uncertainties arising from multiple factors, e.g. model inaccuracies and sensor errors. The addition of such random error provides a more realistic representation of ECG measurements $\mathbf{y}$, and hence, a more realistic representation of inverse solutions. In Equation (1), we added Gaussian noise e as a percent p of the ground-truth ECG torso surface observations, $\mathbf{y}^*$, as

$$p = 100\,\frac{\|\mathbf{e}\|_2}{\|\mathbf{y}^*\|_2}. \tag{2}$$

The forward problem estimates the torso surface potential $\mathbf{y}$ given $\mathbf{h}$, and the inverse problem estimates $\mathbf{h}$ given $\mathbf{y}$.

In recent years, researchers and clinicians have used ECGI to study a variety of arrhythmias, including re-entrant pathways (Ghosh et al. 2008a) and ectopic heart beats (Wang et al. 2011c). ECGI may improve ablation therapy, but researchers do not have a good understanding of how small errors arising from ECG measurements, geometric approximations from imaging, and modelling assumptions for solving the underlying equations affect source localisation in ECGI. Recent work by Tate et al. (2021) on quantifying geometric uncertainty resulting from variations in segmentation has shown some correlation

CONTACT Dennis K. Njeru dnjeru@sci.utah.edu Scientific Computing and Imaging (SCI) Institute, University of Utah, Salt Lake City, USA

between pericardial potential reconstructions and segmentation variability except in the posterior region of the heart.

Understanding uncertainties relevant to computational pipelines is a top research challenge in medical visualisation (Karayiannis et al. 2004; Ristovski et al. 2014; Athawale et al. 2019; Fikal et al. 2019), as well as the visualisation research field in general (Johnson and Sanderson 2003; Brodlie et al. 2012). Recently, visualisations were proposed by Burton et al. (2013) to study uncertainty associated with cardiac forward and inverse problems for 3D volumetric data. In our work, we explore new techniques to visually analyse and understand the uncertainty in epicardial surface data from ECGI simulations.

Building on preliminary work for source localisation by France and Johnson (2016), we apply iterative Krylov methods with Monte Carlo error propagation to study the impact of ECG measurement errors on inverse solutions. We then propose a framework for deriving source localisation confidence interval (CI) regions, and present applications of level-set and topology-based visualisations to visually analyse uncertainty in source localisation. We propose that our CI visualisations could provide a sequential search strategy for clinicians in locating pathological heart beats during ablation therapy. Our level-set and topology-based visualisations can be useful in performing qualitative assessment of inverse solutions and extracting likely source positions.

We organise our paper as follows: In Section 2, we outline the mathematical framework for formulating and solving the inverse problem of electrocardiography. Section 3 discusses our Monte Carlo propagation strategy for studying the uncertainty of ECGI solutions. Section 4 describes our algorithms for developing probability maps and CI regions, as well as applications of level-set and topology-based techniques, for studying uncertainty in source localisation. In Section 5, we show our results and discuss their implications. Finally, in Section 6, we present a summary and propose future work.

2. Inverse problem of electrocardiography

Here we describe the mathematical model, challenges in solving the inverse problem, our regularisation algorithms, and the simulation setup.

2.1. Mathematical model

The potential-based forward and inverse problems of electrocardiography are typically modelled using Laplace's equation (Johnson 1997, 2015; Wang et al. 2011a, 2011b). In our mathematical model, the potential u within a torso is modelled as a function of position x as

$$\cdot\,(\sigma(\mathbf{x})\quad \mathbf{u}(\mathbf{x}))=0,\quad \mathbf{x}\in\Omega \tag{3}$$

$$u(\mathbf{x})=\mathbf{h},\quad \mathbf{x}\in\Gamma_H \tag{4}$$

$$\vec{n}\cdot\sigma(\mathbf{x})\quad u(\mathbf{x})=0,\quad \mathbf{x}\in\Gamma_T \tag{5}$$

where Ω refers to the torso volume, Γ_H denotes the epicardial surface, and Γ_T indicates the torso surface. In this formulation, $\sigma(\mathbf{x})$ is the electrical conductivity tensor, and $\vec{n}$ refers to the unit normal pointing outward from the torso surface, with Equation (5) stating no electric flux leaves the body into the air (Johnson 1997; Wang et al. 2011a, 2011b). Since our main contribution is visualising uncertainty, we have implemented a simplified inverse model. We note that the visualisation techniques we illustrate can be applied to any ECGI pipeline.

Several numerical methods exist for solving Equation (3–5). In this study, we used the finite element method to solve Equation (3–5) and rearranged the resulting stiffness matrix to form the transfer matrix A as described previously in Wang et al. (2011a, 2011b) and Johnson (1997, 2015) to generate Equation 1.

2.2. Ill-posedness and ill-conditioning

In our study, Equation (1) suffers from the ill-posedness common to inverse problems. Equation (1) is ill-posed because small changes in the observed ECG torso surface recordings lead to correspondingly large changes in the reconstructed heart surface potentials. In the discrete approximation, matrix A is highly ill-conditioned, and the singular values of A decay rapidly towards machine precision. Consequently, performing inversions using conventional routines greatly amplifies the impact of any numerical or measurement errors (Wang et al. 2011a, 2011b). To overcome the challenges associated with the ill-posedness and ill-conditioning, researchers employ regularisation (Hansen 2010; Borra`s and Chamorro-Servent 2021). In this paper, to increase the speed and scalability for Monte Carlo sampling, we used iterative methods to regularise solutions in Equation (1), as we describe next.

2.3. Regularisation

In this study, we applied iterative regularisation using the conjugate gradient least squares (CGLS) and preconditioned CGLS (PCGLS) methods. Milanič et al. (2014) have shown that the CGLS method performs as well as the standard Tikhonov methods in solving the ECG inverse problem with single dipole sources, but with the advantage of being computationally more efficient.

2.3.1. Conjugate-Gradient Least Squares (CGLS)

The conjugate gradient least squares (CGLS) algorithm seeks the regularised solution after k iterations, $\mathbf{h_k}$, as demonstrated by Hestenes and Stiefel (1952) and Hansen (2010):

$$\mathbf{h_k}=\text{argmin}_{\mathbf{h}}=\|\,A\mathbf{h}-\mathbf{y}\|_2\; s.t.\;\mathbf{h}\in\mathcal{K}_k \tag{6}$$

where $\mathcal{K}_k$ represents the k^{th} Krylov subspace, which is formally defined as

$$\mathcal{K}_k\equiv span\{A^T\mathbf{y},\,(A^TA)A^T\mathbf{y},\ldots,(A^TA)^{k-1}A^T\mathbf{y}\}. \tag{7}$$

Starting from the zero vector at iteration zero, $\mathbf{h}_0$, this algorithm applies one multiplication with A and A^T per iteration. The solution is formed as a linear combination of the Krylov vectors, and it becomes increasingly enriched in the direction of the principal eigenvector of A^TA (Hansen 2010).

2.3.2. Preconditioned Conjugate-Gradient Least Squares (PCGLS)

We also solved Equation (1) with the preconditioned CGLS (PCGLS) algorithm, using the Laplacian operator L over the heart surface as the right preconditioner. The matrix L was formed as described in Huiskamp and van Oosterom (1988). Because L has a nontrivial null-space W, the PCGLS method requires formation of the A-weighted pseudo-inverse of L (Hansen 2010),

$$L^{\#} = (I - W(AW)^{\dagger}A)L^{\dagger}, \tag{8}$$

where I is the identity matrix. The component of $\mathbf{h_k}$ that exists in the null space of L is given as

$$\mathbf{h}_{\mathcal{N}} = W(AW)^{\dagger}. \tag{9}$$

Then, defining $\bar{\mathbf{y}}$ as

$$\bar{\mathbf{y}} = \mathbf{y} - A\mathbf{h}_{\mathcal{N}}, \tag{10}$$

and with $\bar{A} = AL^{\#}$, we solved $\bar{A}\mathbf{z} = \bar{\mathbf{y}}$ for $\mathbf{z_k}$ using the traditional CGLS routine. The PCGLS solution can then be obtained as

$$\mathbf{h_k} = L^{\#}\mathbf{z_k} + \mathbf{h}_{\mathcal{N}}. \tag{11}$$

As in the CGLS routine, the PCGLS algorithm terminates at some iteration to prevent under-regularisation (Hansen 2010).

2.3.3. Choosing the iteration parameter

In choosing the solution at which to stop iterations, we used both the norm of the residual and the norm of the solution. In using the norm of the residual, we used the Morozov discrepancy principle, in which we stopped the iterations as soon as the norm of the residual was approximately equal to some constant γ times the norm of the noise $\| \mathbf{e}\|_2$, or $\gamma \| \mathbf{e}\|_2$ (Kaipio and Somersalo 2004; Hansen 2010). Following the example of the study by Calvetti et al. (2015), we used $\gamma = 1.2$.

However, as we discuss in our results in Section 5, the discrepancy principle may severely under-regularise the solution when the modelling error is significant relative to the measurement error. To address this under-regularisation, we used physiologically based mathematical constraints for the norm of the solution in limiting the termination iteration k for the CGLS and PCGLS algorithms. Specifically, previous studies on cardiac electrograms recorded and derived relationships on the scalar gain G, between the ℓ_2 norm of the torso and heart voltages at a moment in time, or $\| \mathbf{h}\|_2 \approx G \| \mathbf{y}\|_2$.

These studies had an equal number of torso and heart nodes (i.e. $m = n$) (Davenport et al. 1995; Davenport 1995). To account for differences in the number of heart and torso nodes in this study, we used a slightly modified formula of $\| \mathbf{h}\|_2 \approx G \| \mathbf{y}\|_2\sqrt{n}$ and a gain value G of 7.6, a value slightly less than the maximum experimentally derived value from the ℓ_2 norm in the scalar gain studies (Davenport et al. 1995; Davenport 1995). Putting restrictions on the norm of the solution prevents under-regularisation, particularly when the modelling error exceeds external noise error. Furthermore, slight over-regularisation in inverse reconstructions seems to be preferred for clinical applications as opposed to any form of under-regularisation (Milanič et al. 2014).

2.4. Simulation setup

Figure 1 illustrates the heart in torso geometry (left) and the 250-uniform-ECG-electrode-measurement configuration (right) used in this study. Other studies use a similar electrode configuration and number of electrodes (Ghosh et al. 2008a; Rudy 2013).

For this study, we added noise from 0.01% to 3%, values similar to those found in other studies (Burnes et al. 2000; Wang et al. 2011a, 2011b, 2013). Additionally, we used a different transfer matrix A in forming the ground-truth observations $\mathbf{y}^*$ compared with the transfer matrix used in inversions to avoid so-called 'inverse crime', where the solution is biased by using the same mesh for forward and inverse simulations (Kaipio and Somersalo 2007). For the forward model simulation, we utilised a higher resolution finite element model as illustrated in Table 1. We use a single stimulation point for our analysis throughout the paper. Additionally, for our inverse simulations, we added 2 mm Gaussian geometric error to the torso surface recording sites, as in other studies (Burnes et al. 2000).

Figure 1. Inversions utilized the heart torso geometry (left) with a 250-uniform-lead configuration (right).

Table 1. Forward and inverse model resolution.

Number of Attributes	Forward Model	Inverse Model
elements	128,898	75,605
heart nodes	3,573	2,206
torso nodes	7,328	4,754

3. Monte Carlo approach to studying solution uncertainty

Having obtained an initial solution $\mathbf{h_k}$ using the CGLS or PCGLS routine, we forward-propagated the solution to form an assumed noise-free right-hand side $\tilde{\mathbf{y}}$ with

$$\tilde{\mathbf{y}} = A\mathbf{h_k}, \tag{12}$$

as described in Aster et al. (2013). To perform Monte Carlo error analysis, we sampled a noisy solution $\mathbf{y_s} \sim \mathcal{N}(\tilde{\mathbf{y}}, \sigma^2\mathbf{I})$, where σ represents the standard deviation of the noise, a value that was fixed to produce errors at the same percentage p as in the original Equation (1). We then used the CGLS and PCGLS routines to obtain individual inversion samples, just as we obtained h_k in originally solving Equation (1) (Aster et al. 2013; France and Johnson 2016). We obtained an ensemble of 200 Monte Carlo samples per simulation.

4. Visualising source localization uncertainty

We analysed the uncertainty in source localisation across 200 Monte Carlo samples per simulation via probability maps, confidence interval regions, level-set visualisations, and topology-based visualisations.

4.1. Probability maps

For probabilistic maps, similar to the early study by France and Johnson (2016), we located the top 3% of the lowest voltage values (with the lowest voltage denoting the source (Wang and Rudy 2006)), and averaged these locations over the 200 samples to form a probabilistic representation for source localisation. In France and Johnson (2016), probabilistic maps were visualised with direct mapping of probability to opacity. In our probabilistic map visualisations, we used colour maps to segment the regions of high probability (>0.75), moderate probability (between 0.5 and 0.75/between 0.25 and 0.5), and low probability (<0.25). We propose that the segmented visualisations can potentially benefit clinicians in performing sequential searches for source localisation.

4.2. Confidence intervals

Although probability maps represent the probability mass function for source localisation, the confidence interval regions may be considered as the corresponding cumulative density function for source localisation. To generate these visualisations for confidence intervals, we performed integration of the probability maps from the position of the estimated source location. First, we determined the estimated source location, along with the probability maps. For each node, we assigned the confidence interval value at a particular node i, which is the value of the sum of the probabilities that reside within the radius from the estimated source location to that node i. After calculating the confidence interval values at each node, we divided the 25%, 50%, and 75% confidence interval regions using contour lines via the marching triangles algorithm (Hilton and Illingworth 1997). Again, the bands visualised with confidence interval visualisations can potentially help clinicians perform sequential searches for source localisation.

4.3. Level-set visualizations

We perform level-set visualisations to identify the regions that could contain the source of arrhythmia. Level-sets (Lorensen and Cline 1987) are a fundamental surface-based visualisation technique for gaining insight from complex scientific data. Mathematically, for a function f: $\mathbb{R} \rightarrow \mathbb{R}$ defined on a d-dimensional manifold, its level-set S for isovalue c is defined as $S = \{x \in \mathbb{R} | f(x) = c\}$. Figure 2b illustrates level-sets of a synthetic Ackley function (Ackley 1987) shown in Figure 2a. The level-sets in Figure 2b for different isovalues c are displayed in different colours. In the ECGI context, function f is a mapping from nodes of a mesh representing the heart surface to inverse solutions denoting epicardial potentials. We investigate level-sets with relatively low isovalues to understand potential positions of arrhythmia.

We guide our selection of an isovalue for level-set visualisations using parallel coordinate (Inselberg 1985) and histogram plots. Parallel coordinate plots are a well-known visualisation technique to study correlation among dimensions of multivariate data. For our analysis, in the parallel coordinate plot, we treat each node of a mesh representing the heart surface as a single dimension of a parallel coordinate plot. We then plot the potentials across all nodes and 200 samples. Likewise, in the histogram plot, cardiac potentials across all nodes and 200 samples are grouped into bins. We then use these plots to gain insight into the relatively low potential values that are observed across all samples. We pick one of the low potential values as the isovalue for level-set rendering. Level-sets with relatively low isovalues help us extract regions that correspond to a potential source (Wang and Rudy 2006). Finally, we visualise isocontours for the selected isovalue using spaghetti plots (Potter et al. 2009) and isocontour variation plots (Whitaker et al. 2013).

4.4. Topology-based visualizations

Topological data analysis is a powerful tool for understanding complex simulation datasets (Miller et al. 2006; Bremer et al. 2010). We propose visualisations of topological abstractions, specifically, critical points and Morse complexes (Edelsbrunner et al. 2001), of CGLS and PCGLS inverse solutions to gain insight into the likely source positions and their variations. Let function f: $\mathbb{R} \rightarrow \mathbb{R}$ be defined on a d-dimensional manifold, and let ∇f denote its gradient field. A point x on a manifold is considered critical if $\nabla f = 0$. Given a Morse function f defined on a d-dimensional manifold, i.e, a function with no flat regions, the Morse complex of f decomposes the manifold into regions (referred to as cells) with uniform gradient behaviour. Figure 2c illustrates the Morse complex segmentation of the Ackley function shown in Figure 2a. In Figure 2c, nine Morse complex cells

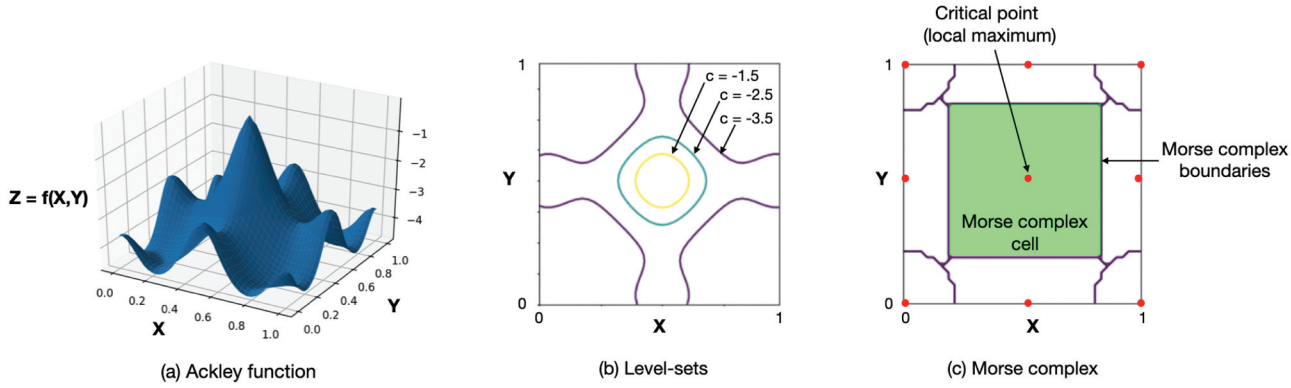

Figure 2. Illustration of level-sets in image (b) and Morse complexes in image (c) for the synthetic Ackley function *f* depicted in image (a). Level-sets are visualized for different isovalues *c*. The Morse complex visualization denotes nine cells (a single cell highlighted in green) corresponding to nine critical points (local maxima indicated by red dots) of the Ackley function. Gradients within a single cell flow to its corresponding critical point.

correspond to nine critical points of (local maxima) of the Ackley function. In our case, the Morse complexes segment the heart surface into cells, where gradients within a single cell terminate in a single local minimum associated with a cell (also known as an ascending manifold). Thus, local minima of ECGI solutions provide insight into the positions that have the smallest potential within their local neighbourhood (represented by the Morse complex cell), thus indicating potential source positions.

5. Results and discussions

We now present results for each visualisation technique described in Section 4 to understand the source localisation uncertainty.

5.1. Probability and confidence maps

We first present the uncertainty visualisation results using probability maps and our proposed confidence maps in Figure 3. Figure 3a visualises the ground-truth heart surface voltages (in mV). In all plots, the white dot indicates the position of the ground-truth source. Figures 3(b,c) visualise the CGLS and PCGLS inverse solutions at 1.5% external noise for a single Monte Carlo sample.

Figures 3(b,c) illustrate the challenges in obtaining inverse solutions in ECGI, i.e. the reconstructed voltages in Figures 3(b, c) differ significantly in both range and magnitude in comparison to the ground-truth, Figure 3a. This difference is evidence of the significant ill-conditioned nature of discrete ECGI problems, as discussed in Section 2.2. Inversions in Figure 3(b,c) were performed with the lower resolution 'Inverse Model' mesh

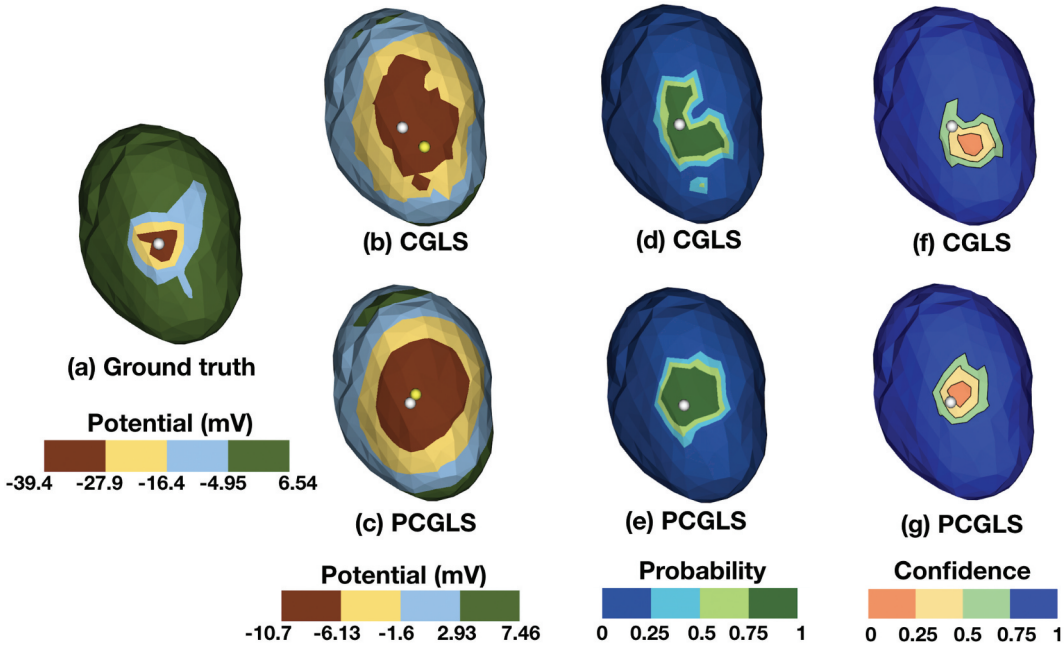

Figure 3. Uncertainty analysis of Monte Carlo simulations with probabilistic and confidence maps: (a) the ground-truth voltages, (b,c) the CGLS and PCGLS inversions for a single Monte Carlo sample at 1.5% external noise, (d,e) probabilistic maps, (f,g) confidence maps. The white dots denote the true source positions, whereas the yellow dots in (b,c) denote the estimated source positions. The results (a-c) are colormapped with the potential values, the results (d,e) are colormapped with the probabilities, and the results (f,g) are colormapped with the confidence values.

in Table 1, and with additive 2 mm Gaussian geometric error on the heart surface, as described in Section 2. The yellow dot in Figure 3(b,c) indicates the estimated source location for each individual visualisation. This yellow dot corresponds to the global minima of the reconstructed epicardial potentials.

Figures 3(d,e) and Figure 3(f,g) illustrate the probability maps (France and Johnson 2016) and confidence maps, respectively. For the probability maps visualised in Figure 3(d,e), the darker green areas indicate the regions of higher probability for source localisation. In the confidence maps visualised in Figure 3(f–g), the contour lines separate the 25% (orange), 50% (yellow), and 75% (light green) CI regions for source localisation. Specifically, in the orange regions, our model states that the probability of finding the source is less than or equal to 25%. Likewise, the probability of finding the source in the combined orange and yellow regions is less than or equal to 50%. Note the lack of symmetry around the sites of stimulation, which is due to the coarseness of the grid and its unstructured nature.

The green region representing the high source localisation probability in probabilistic maps (Figure 3(d,e)) still covers a relatively large surface area. The CI visualisations could provide clinicians with an improved sequential search strategy for planning ablation therapy. For example, during an ablation procedure, a clinician might sequentially search the 25%, 50%, and 75% CI regions to locate the source of cardiac tissue responsible for spontaneous pathological heart beats or re-entrant wave activity.

The vertex positions of confidence/probability map contours can be utilised to quantify the positional uncertainty of source localisation. For example, in Figure 3g, the maximum Euclidean distance between contour vertices for the 25% confidence interval is 8.56 mm. The error in source localisation, thus, may not exceed 8.56 mm, assuming that the 25% confidence region is locally planar and the source resides in the 25% confidence region. More advanced techniques of error quantification may be developed in the future that take into account contour vertex positions and heart surface curvature.

Figure 4 illustrates probability maps for the CGLS and PCGLS routines at various external noise levels, as defined in Equation (2). In both algorithms, the probability tended to aggregate around the ground-truth source location until approximately 3% external noise. Figure 5 illustrates the corresponding CI regions for the CGLS and PCGLS routines. For the CGLS and PCGLS routines, the ground-truth source location fell within the 50% CI region (yellow) and 25% CI region (orange), respectively, for all noise levels.

Figure 6 illustrates the convergence of the CGLS routine at 0.5% and 2.5% external noise levels, both with and without modelling error using the CGLS algorithm. Although not shown, PCGLS gives similar results. At 0.5% external noise (Figure 6, left), the norm of the residual approaches the norm of the noise after 20 iterations to satisfy the Morozov discrepancy principle. However, in the presence of modelling error in the transfer matrix A (from a coarser mesh resolution and torso surface electrode position errors, as described in Section 2), the CGLS residual does not converge to the norm of the external noise, even after several hundred iterations (not shown). At 2.5% noise, however (Figure 6, right), the convergence patterns of CGLS on transfer matrices with and without modelling error follow a nearly identical pattern. Figure 6 (left) illustrates the need to also use the norm of the solution as a constraint to prevent under-regularisation, especially when the ratio of modelling error to external error is large. Other studies also report difficulties in regularisation when modelling error exceeds measurement error (Johnston and Gulrajani 2002).

5.2. Level-set visualizations

Next, we study the source localisation uncertainty by extracting level-sets of epicardial potentials, in which we guide the isovalue selection with parallel coordinate plots and histograms. Figure 7 shows a parallel coordinates plot (left) and a histogram (right) plot of the 200 samples denoting the epicardial voltage recordings at each of the 337 heart nodes represented at the 0.5% noise level. A parallel coordinate plot has the advantage of not losing spatial context as opposed to a histogram. These

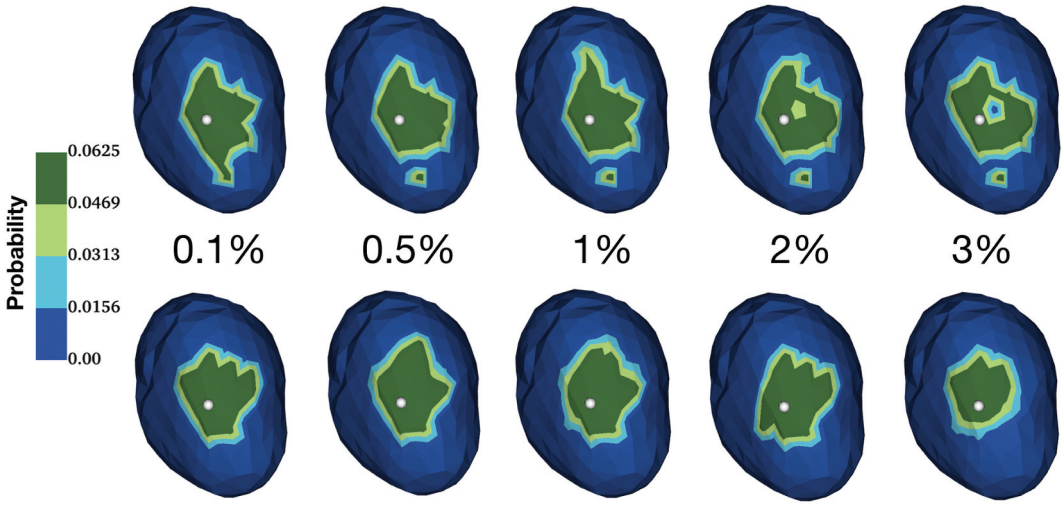

Figure 4. Probability maps for source localization illustrate uncertainty as a function of noise in ECG observations for the CGLS inversion (top row) and PCGLS inversion using a Laplacian preconditioner (bottom row). White dots mark the ground-truth source location.

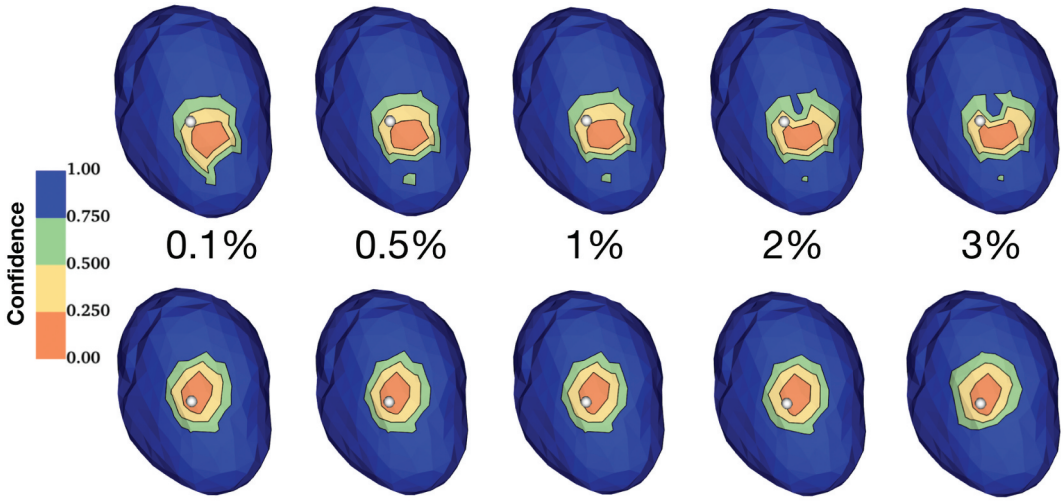

Figure 5. Confidence interval (CI) regions for source localization illustrate uncertainty as a function of external noise in ECG observations for the CGLS inversion (top row) and PCGLS inversion using a Laplacian preconditioner (bottom row). Dots mark the ground-truth source location. Contour lines separate the 25%, 50%, and 75% CI regions.

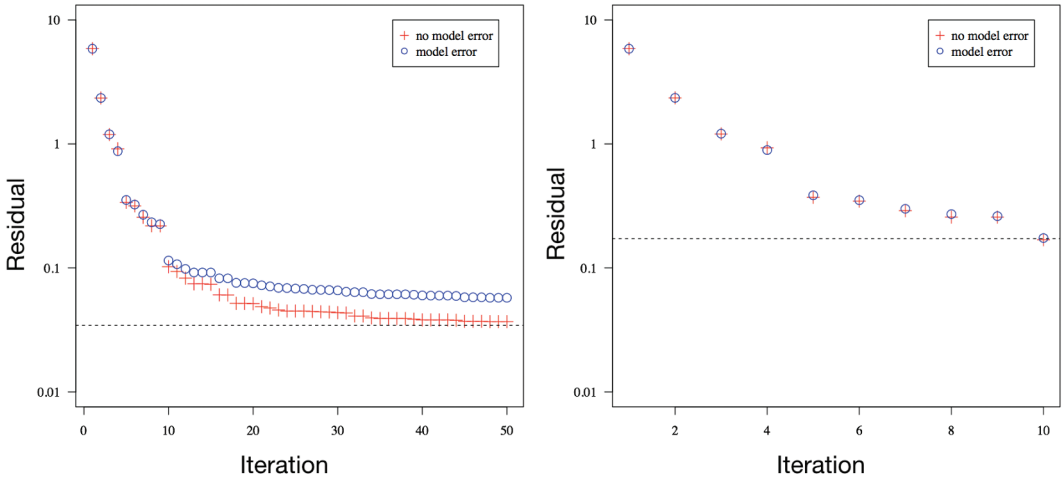

Figure 6. At 0.5% external noise (left), modeling error affects convergence, whereas at 2.5% external noise (right), convergence appears similar both with and without modeling error. For both plots, the dashed line indicates the Morozov discrepancy principle termination criterion.

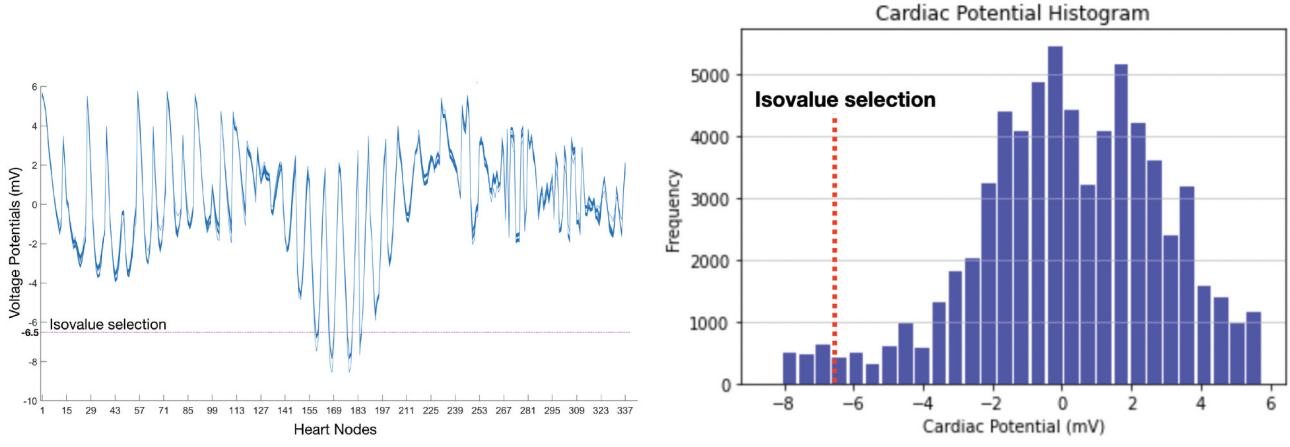

Figure 7. Parallel coordinate (left) and histogram (right) plots of heart surface voltage recordings from 200 Monte Carlo samples at the 0.5% noise level. The dotted lines indicate our isovalue selection (−6.5mv) for level-set rendering.

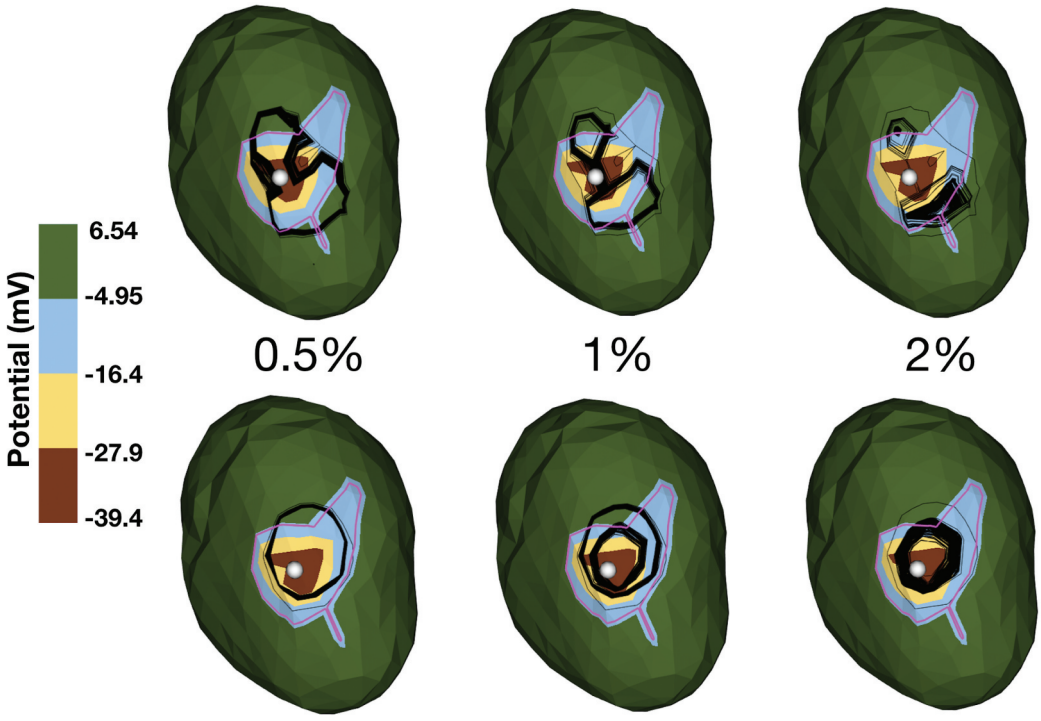

Figure 8. Isocontour maps for sample *isovalue* $= -6.5$ mV showing the ground-truth isocontours (purple) overlaid with isocontours (black) from the 200 samples. The top row shows isocontours without any smoothing (i.E., CGLS) whereas the bottom row shows isocontours with Laplacian smoothing applied (i.E., PCGLS). The columns indicate different noise levels. Dots mark the ground-truth source location.

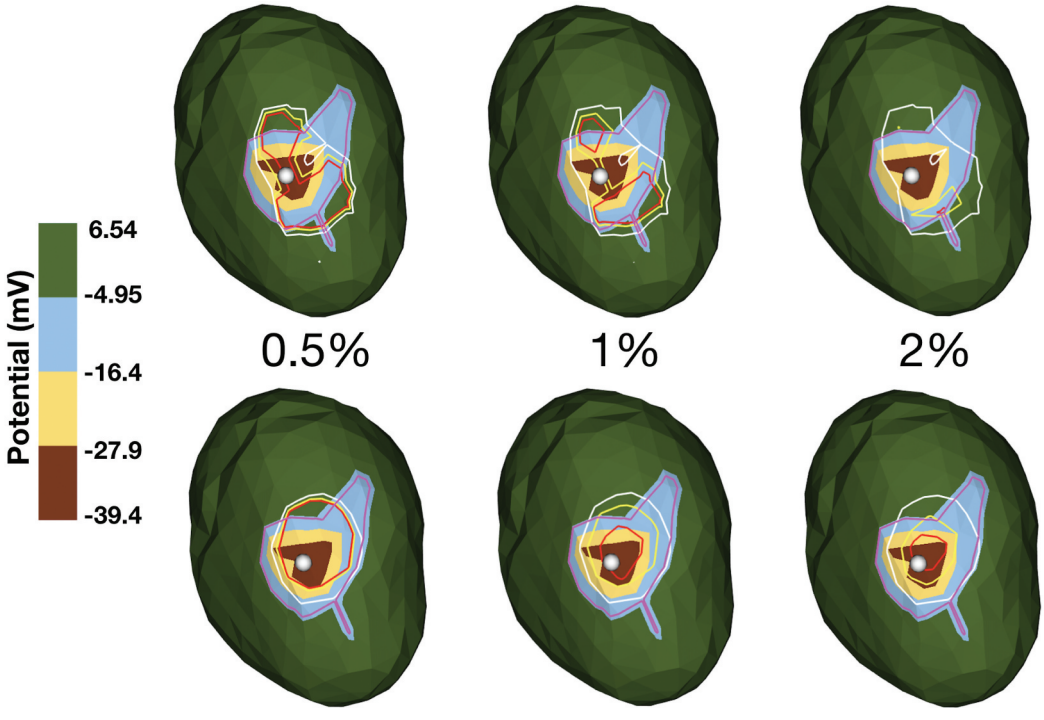

Figure 9. Isocontour maps for sample *isovalue* $= -6.5$ mV showing the ground-truth isocontours (purple) overlaid with the minimum (white), maximum (red), and average (yellow) isocontours from the 200 samples at each noise level. The top row shows isocontours without any smoothing (i.E., CGLS) whereas the bottom row shows isocontours with Laplacian smoothing applied (i.E., PCGLS). The columns indicate different noise levels.

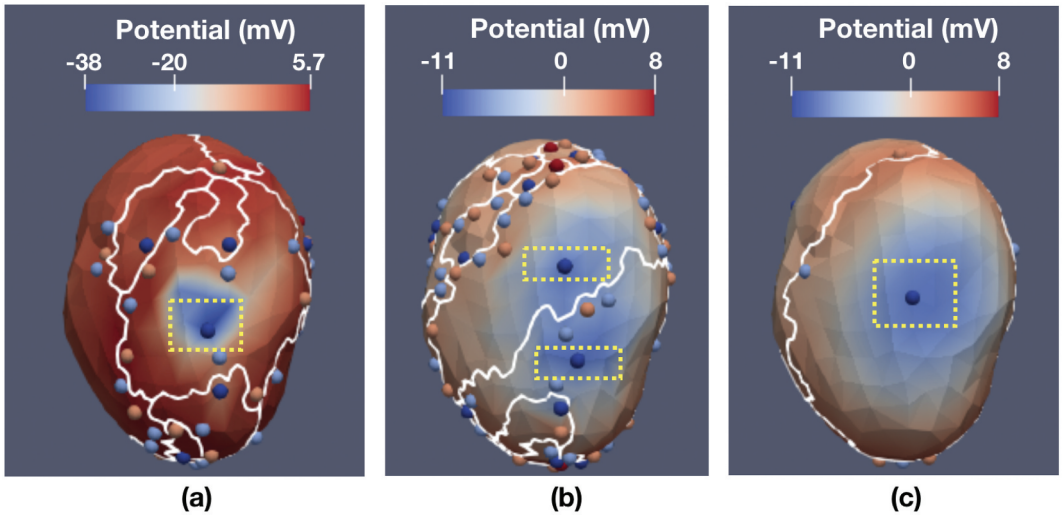

Figure 10. Visualization of Morse complexes and critical points for (a) ground-truth, (b) CGLS at 1% noise, and (c) PCGLS at 1% noise. The white contours denote the Morse complex cells, the dark blue spheres denote the local minima associated with each Morse complex cell, and the orange spheres denote local maxima of respective fields. The potential values are colormapped on the heart surface. The local minimum enclosed by the bottom yellow box in the CGLS visualization is situated closer (6.55 mm) to the true solution, indicated by the yellow box in the ground-truth, when compared to the PCGLS solution (7.72 mm).

plots were useful in the visualisation and selection of the low-magnitude heart surface voltages corresponding to the sources, as described in Section 4. We used these plots in choosing the isovalue −6.5 mV.

Figure 8 shows a spaghetti plot of level-set renderings for the isovalue −6.5 mV across different noise levels. As can be observed, the ground-truth source location fell within the confines of level-sets for all noise levels. Thus, the region represented by the outermost level-set of a spaghetti plot denotes the likely existence of a source location. In Figure 8, the isocontour shape for the PCGLS solutions (bottom row) appears more closely aligned with the ground-truth isocontour (purple) shape when compared to the shape of the CGLS isocontours (top row).

We visualise an isocontour variation plot to reduce the clutter caused by spaghetti plots. Figure 9 visualises the variations corresponding to the spaghetti plots shown in Figure 8. Figure 9 may be easier to analyse and provides a less cluttered visualisation because the 200 samples are summarised by the minimum (white), maximum (red), and average (yellow) isocontours overlaid on the ground-truth (purple). The minimum isocontour refers to the isocontour generated by using the minimum value from the reconstructed voltage potentials across all simulations. Likewise, the maximum isocontour refers to the isocontour generated by using the maximum value from the reconstructed voltage potentials, and the average isocontour refers to the isocontour generated by using the average value from the reconstructed voltage potentials. These isocontours are then overlaid on the ground-truth. This approach significantly reduces clutter while clearly showing the variation, and therefore, uncertainty, contained in the reconstructed solutions.

5.3. Topology-based visualizations

Lastly, we analyse the source uncertainty via visualisation of critical points and Morse complexes derived from ECGI solutions. Figure 10a visualises the critical points (spheres) and Morse complex (white contours) for the ground-truth. Similar visualisations are produced for the CGLS (Figure 10b) and PCGLS (Figure 10c) solutions for the 1% noise level and a single sample. The visualisations are performed in ParaView (Ayachit 2015) using the topology toolkit (Tierny et al. 2018). The local minima of all three fields are visualised with the dark blue spheres, and the local maxima are visualised with the orange spheres. As indicated in Figure 9b, there are two local minima (enclosed by yellow dotted boxes), indicating uncertainty in source positions. However, this uncertainty can be further reduced by employing better regularisation schemes, e.g. PCGLS, as shown in Figure 10c. Even though Figure 10 visualises critical points for the sample 50, a similar trend is observed across all simulations.

6. Conclusion and future work

In this paper, we use multiple visualisation techniques, several of which are new to ECGI applications, to study the impact of measurement and modelling errors associated with the ECGI pipeline on epicardial source localisation. Specifically, we present applications of confidence maps, level-sets, and topology-based visualisations for effective analysis of uncertainty in source localisation. In the future, we would like to study the sensitivity of source localisation to variations in other ECGI parameters, such as electrical conductivity and number and configuration of ECG leads. We would also like to study and visualise uncertainties arising from multiple sources and add a quantitative metric to our probability maps and confidence maps to reflect the multiple localisation errors resulting from multiple pacing site estimations. The analysis for multiple sources would require additional research into more sophisticated statistical models and uncertainty visualisations and would be an interesting extension of the methods presented here. Lastly, we would like to study how the different

visualisation methods we presented compare under different arrhythmia scenarios.

Note

1. This manuscript has been authored by UT-Battelle, LLC under Contract No. DE-AC05-00OR22725 with the U.S. Department of Energy. The publisher, by accepting the article for publication, acknowledges that the U.S. Government retains a non-exclusive, paid up, irrevocable, world-wide licence to publish or reproduce the published form of the manuscript, or allow others to do so, for U.S. Government purposes. The DOE will provide public access to these results in accordance with the DOE Public Access Plan (http://energy.gov/downloads/doe-public-access-plan).

Acknowledgments

The authors would like to give special thanks to Professor Rob MacLeod for generously sharing the electrocardiogram data.

Disclosure statement

No potential conflict of interest was reported by the author(s).

Funding

This project was supported by grants from the National Institute of General Medical Sciences (P41 GM103545-18, R24 GM136986) and the Intel Graphics and Visualization Institutes of XeLLENCE, the Scientific Discovery through Advanced Computing (SciDAC) program in the U.S. Department of Energy. The authors would like to give special thanks to Professor Rob MacLeod for generously sharing the electrocardiogram data.

ORCID

Dennis K. Njeru http://orcid.org/0000-0001-8934-4130
Tushar M. Athawale http://orcid.org/0000-0003-3163-6274

References

Ackley DH. 1987. A connectionist machine for genetic hillclimbing. Norwell, MA, USA: Kluwer Academic Publishers.

Arya A, Hindricks G, Sommer P, Huo Y, Bollmann A, Gaspar T, Bode K, Husser D, Kottkamp H, Piorkowski C. 2010. Long-term results and the predictors of outcome of catheter ablation of atrial fibrillation using steerable sheath catheter navigation after single procedure in 674 patients. Eurospace. 12(2):173–180. doi:10.1093/europace/eup331.

Aster RC, Borchers B, Thurber CH. 2013. Parameter estimation and inverse problems. 2nd ed. Boston: Elsevier Incorporated.

Athawale TM, Johnson KA, Butson CR, Johnson CR. 2019. A statistical framework for quantification and visualisation of positional uncertainty in deep brain stimulation electrodes. Comput Methods Biomech Biomed Eng Imaging Vis. 7(4):438–449.

Ayachit U. 2015. The paraview guide: a parallel visualization application. USA: Kitware, Inc.

Borra`s M, Chamorro-Servent J. 2021. Electrocardiographic imaging: a comparison of iterative solvers. Front Physiol. 12:620250. doi:10.3389/fphys.2021.620250.

Bremer PT, Weber G, Pascucci V, Day M, Bell J. 2010. Analyzing and tracking burning structures in lean premixed hydrogen flames. IEEE Trans Vis Comput Graph. 16(2):248–260. doi:10.1109/TVCG.2009.69.

Brodlie K, Allendes RO, Lopes A. 2012. A review of uncertainty in data visualization. Expanding Front Visual Anal Visualization. 81–109.

Burnes JE, Taccardi B, Rudy Y. 2000. A noninvasive imaging modality for cardiac arrhythmias. Circulation. 102(17):2152–2158. doi:10.1161/01.CIR.102.17.2152.

Burton B, et al. 2013. Uncertainty visualization in forward and inverse cardiac models. In: Computing in Cardiology Conference Zaragoza, Spain. IEEE Press. p. 57–60.

Calvetti D, Pitolli F, Somersalo E, Vantaggi B. 2015. Bayes meets Krylov: preconditioning CGLS for underdetermined systems. ArXiv e-prints.

Cluitmans M, Brooks DH, MacLeod R, Dössel O, Guillem MS, van Dam PM, Svehlikova J, He B, Sapp J, Wang L, et al. 2018. Validation and opportunities of electrocardiographic imaging: from technical achievements to clinical applications. Front Physiol. 9:1305. doi:10.3389/fphys.2018.01305. Available from.

Davenport DM. 1995. Temporal, spatial and frequency constraints on heart surface potential distributions [master's thesis]. Northeastern University.

Davenport DM, Brooks DH, MacLeod RS. 1995. Experimentally derived realistic constraints on epicardial potential distributions. In: Proceedings of the 21st N.E. Bioengineering Conference, Bar Harbor, ME, USA. p. 10–12.

Edelsbrunner H, Harer J, Zomorodian A. 2001. Hierarchical Morse complexes for piecewise linear 2-manifolds. In: Proceedings of the 17th Annual Symposium on Computational Geometry, Medford, Massachusetts, USA. p. 70–79.

Fikal N, Aboulaich R, El Guarmah E, El Mahdi, Zemzemi N. 2019. Propagation of two independent sources of uncertainty in the electrocardiography imaging inverse solution. Math Model Nat Phenom. 14(2):206. doi:10.1051/mmnp/2018065.

France J, Johnson CR. 2016. Source localization probability maps for uncertainty quantification in electrocardiographic imaging. Comput Cardiol (CinC). 697–700.

Ghosh S, Avari JN, Rhee EK, Woodard PK, Rudy Y. 2008a. Noninvasive electrocardiographic imaging (ECGI) of a univentricular heart with Wolff-Parkinson-White syndrome. Heart Rhythm. 5(4):605–608. doi:10.1016/j.hrthm.2007.12.018.

Ghosh S, Avari JN, Rhee EK, Woodard PK, Rudy Y. 2008b. Noninvasive electrocardiographic imaging (ecgi) of epicardial activation before and after catheter ablation of accessory pathway in a patient with Ebstein's anomaly. Heart Rhythm. 5(6):857–860. doi:10.1016/j.hrthm.2008.03.011.

Hansen PC. 2010. Discrete inverse problems insight and algorithms. Philadelphia: Society for Industrial and Applied Mathematics.

Hestenes MR, Stiefel E. 1952. Methods of conjugate gradients for solving linear systems. J Res Natl Bur Stand. 49(6):409–436. doi:10.6028/jres.049.044.

Hilton A, Illingworth J. 1997. Marching triangles: Delaunay implicit surface triangulation. University of Surrey. Report No:.

Huiskamp G, van Oosterom A. 1988. The depolarization sequence of the human heart surface computed from measured body surface potentials. IEEE Trans Biomed Eng. 35(12):1047–1058. doi:10.1109/10.8689.

Inselberg A. 1985. The plane with parallel coordinates. Vis Comput. 1(4):69–91. doi:10.1007/BF01898350.

Johnson C. 1997. Computational and numerical methods for bioelectric field problems. Crit Rev Biomed Eng. 25(1):1–81. doi:10.1615/CritRevBiomedEng.v25.i1.10.

Johnson C. 2015. Computational methods and software for bioelectric field problems. In: Bronzino J, and Peterson D, editors. Biomedical engineering handbook. 4th ed. Vol. 1. Boca Raton, FL, USA: CRC Press; p. 1–28; chap. 43.

Johnson CR, Sanderson AR. 2003. A next step: visualizing errors and uncertainty. IEEE Comput Graph Appl. 23(5):6–10. doi:10.1109/MCG.2003.1231171.

Johnston PR, Gulrajani RM. 2002. A new method for regularization parameter determination in the inverse problem of electrocardiography. IEEE Trans Biomed Eng. 44(1):19–39. doi:10.1109/10.553710.

Kaipio J, Somersalo E. 2004. Statistical and computational inverse problems. New York: Springer.

Kaipio J, Somersalo E. 2007. Statistical inverse problems: discretization, model reduction and inverse crimes. J Comput Appl Math. 198(2):493–504. doi:10.1016/j.cam.2005.09.027.

Karayiannis N, Mukherjee A, Glover J, Ktonas P, Frost J, Hrachovy R, Mizrahi E. 2004. Quantifying and visualizing uncertainty in EEG data of neonatal seizures. In: The 26th Annual International Conference of the IEEE Engineering in Medicine and Biology Society, San Francisco, CA, USA. Vol. 1. p. 423–426.

Lorensen WE, Cline HE. 1987. Marching cubes: a high resolution 3D surface construction algorithm. SIGGRAPH Comput Graphics. 21(4):163–169. doi:10.1145/37402.37422.

MacLeod R, Stinstra J, Lew S, Whitaker R, Swenson D, Cole M, Krüger J, Brooks D, Johnson C. 2009. Subject-Specific, multiscale simulation of electrophysiology: a software pipeline for image-based models and application examples. Philos Trans Royal Soc a Math Phys Eng Sci. 367 (1896):2293–2310. doi:10.1098/rsta.2008.0314.

Messineo FC. 1989. Ventricular ectopic activity: prevalence and risk. Am J Cardiol. 64(20):53J–56J. doi:10.1016/0002-9149(89)91200-9.

Milanič M, Jazbinšek V, MacLeod RS, Brooks DH, Hren R. 2014. Assessment of regularization techniques for electrocardiographic imaging. J Electrocardiol. 47(1):20–28. doi:10.1016/j.jelectrocard.2013.10.004.

Miller P, Bremer PT, Cabot W, Cook A, Laney D, Mascarenhas A, Pascucci V. 2006. Application of Morse theory to analysis of Rayleigh-Taylor topology. In: 10th International Workshop on the Physics of Compressible Turbulent Mixing, Paris, France.

O'Donnell D, Furniss SS, Dunuwille A, Bourke JP. 2003. Delayed cure rate despite early recurrence after pulmonary vein isolation for atrial fibrillation. Am J Cardiol. 91(1):83–85. doi:10.1016/S0002-9149(02)03005-9.

Potter K, Wilson A, Bremer PT, Williams D, Doutriaux C, Pascucci V, Johhson CR. 2009. Ensemble-vis: a framework for the statistical visualization of ensemble data. In: IEEE Workshop on Knowledge Discovery from Climate Data: Prediction, Extremes, Miami, FL, USA. p. 233–240.

Ristovski G, Preusser T, Hahn HK, Linsen L. 2014. Uncertainty in medical visualization: towards a taxonomy. Comput Graphics. 39:60–73. doi:10.1016/j.cag.2013.10.015.

Rudy Y. 2013. Noninvasive electrocardiographic imaging of arrhythmogenic substrates in humans. Circ Res. 112(5):863–874. doi:10.1161/CIRCRESAHA.112.279315.

Tate JD, Good WW, Zemzemi N, Boonstra M, van Dam P, Brooks DH, Narayan A, MacLeod RS. 2021. Uncertainty quantification of the effects of segmentation variability in ecgi. In: Ennis D, Perotti L Wang V, editors. Functional imaging and modeling of the heart. Cham: Springer International Publishing; p. 515–522.

Tierny J, Favelier G, Levine JA, Gueunet C, Michaux M. 2018. The topology toolkit. IEEE Trans Vis Comput Graph. 24(1):832–842. doi:10.1109/TVCG.2017.2743938.

van der Graaf AW, Bhagirath P, Ramanna H, van Driel VJ, de Hooge J, de Groot NM, Götte MJ. 2014. Noninvasive imaging of cardiac excitation: current status and future perspective. Ann Noninvasive Electrocardiol. 19(2):105–113. doi:10.1111/anec.12140.

Wang Y, Cuculich PS, Zhang J, Desouza KA, Vijayakumar R, Chen J, Faddis MN, Lindsay BD, Smith TW, Rudy Y. 2011c. Noninvasive electroanatomical mapping of human ventricular arrhythmias with electrocardiographic imaging. Sci Transl Med. 3(98):98ra84. doi:10.1126/scitranslmed.3002152.

Wang D, Kirby RM, Johnson CR. 2011a. Finite-Element-Based discretization and regularization strategies for 3-D inverse electrocardiography. IEEE Trans Biomed Eng. 58(6):1827–1838. doi:10.1109/TBME.2011.2122305.

Wang D, Kirby RM, Johnson CR. 2011b. Resolution strategies for the finite element based solution of the electrocardiographic inverse problem. IEEE Trans Biomed Eng. 57(2):220–237. doi:10.1109/TBME.2009.2024928.

Wang D, Kirby RM, MacLeod RS, Johnson CR. 2013. Inverse electrocardiographic source localization of ischemia: an optimization framework and finite element solution. J Comput Phys. 250:403–424. doi:10.1016/j.jcp.2013.05.027.

Wang Y, Rudy Y. 2006. Application of the method of fundamental solutions to potential-based inverse electrocardiography. Ann Biomed Eng. 34 (8):1272–1288. doi:10.1007/s10439-006-9131-7.

Whitaker R, Mirzargar M, Kirby R. 2013. Contour boxplots: a method for characterizing uncertainty in feature sets from simulation ensembles. IEEE Trans Vis Comput Graph. 19(12):2713–2722. doi:10.1109/TVCG.2013.143.